

NUMERICAL SIMULATION OF DUST AGGREGATE COLLISIONS. I. COMPRESSION AND DISRUPTION OF TWO-DIMENSIONAL AGGREGATES

KOJI WADA, HIDEKAZU TANAKA, TORU SUYAMA, HIROSHI KIMURA, AND TETSUO YAMAMOTO

Institute of Low Temperature Science, Hokkaido University, Sapporo 060-0819, Japan; wada@neko.lowtem.hokudai.ac.jp

Received 2006 December 8; accepted 2007 February 13

ABSTRACT

We carry out numerical simulations of dust aggregate collisions to study the compression and disruption processes of aggregates in their growth. To compare with the pioneering studies of Dominik & Tielens, we focus on two-dimensional head-on collisions, in which we obtain similar results for compression and disruption to theirs. In addition to the similarities, we examine the dependence of the collisional outcomes on the aggregate size and the parameters relevant to the particle interaction in detail by treating large aggregates that consist of up to 2000 particles. Compression of aggregates by collisions reduces the radius of gyration and increases the number of contacts between the constituent particles. Our results show that the changes in the gyration radius and the number of contacts after impact depend on the impact energy and that the dependence is scaled by the energy necessary to roll all contacts. We provide empirical formulae for the changes in the gyration radius and the number of contacts. Furthermore, we find that the degree of maximum compression is determined by the ratio of rolling energy to breaking energy. This indicates that ice aggregates become more compact than quartz aggregates in the same impact conditions. Any aggregates are catastrophically disrupted when the impact energy exceeds approximately 10 times the energy necessary to break all contacts. Our results, however, suggest that it becomes harder to disrupt the aggregates with an increasing number of particles.

Subject headings: circumstellar matter — dust, extinction — methods: *n*-body simulations —
 planetary systems: formation — planetary systems: protoplanetary disks

1. INTRODUCTION

The structure of dust aggregates is an important parameter for understanding planetesimal formation processes and analyzing observational data from protoplanetary disks. For example, the structure of dust aggregates determines their cross sections and the gas drag forces on them, which strongly affect their motion and collisional growth in a protoplanetary disk (e.g., Weidenschilling 1980, 1984; Nakagawa et al. 1981; Tanaka et al. 2005). The coupling of dust with disk gas is an important factor in planetesimal formation through gravitational instability of the dust layer (e.g., Weidenschilling & Cuzzi 1993). In observations of protoplanetary disks, on the other hand, much information about disks could be derived from dust thermal emission. Thermal emission properties of dust aggregates are strongly dependent on their structures (e.g., Wright 1987; Stognienko et al. 1995; Min et al. 2003, 2005, 2006). Hence, we need a reliable model of dust structure to derive accurate information from disk observation.

The structure of dust aggregates is dependent on the processes of their collisional growth. When aggregates of comparable size collide with a sufficiently low relative velocity ($\lesssim 1 \text{ cm s}^{-1}$), fluffy aggregates called ballistic cluster-cluster aggregations (BCCAs) are formed (e.g., Meakin 1991). This is the case in the early stage of dust growth in protoplanetary disks, because of their strong coupling with disk gas (e.g., Adachi et al. 1976). If the collision velocity is so high as to compress the colliding aggregates, on the other hand, they would grow to compact aggregates. Hence, it is necessary to examine the evolution of dust structure in the course of their growth; in particular, it is important to clarify when and how aggregates are compressed. Most previous studies of dust growth in protoplanetary disks assumed compact aggregates and did not consider structure evolution. Some studies of dust growth took into account structure evolution (e.g., Ossenkopf 1993; Weidenschilling & Ruzmaikina 1994; Kempf et al. 1999; Blum

2004; Ormel et al. 2007). However, further study of the structure evolution is required to construct a reliable model of dust growth. As a first step toward such a dust model, one needs to examine dust aggregate collisions with direct *N*-body simulations.

Dominik & Tielens (1997) carried out a comprehensive numerical simulation of aggregate collisions. They modeled particle interactions in detail and calculated the motion of each particle directly in their simulation. As a result, they derived a simple recipe for outcomes of aggregate collisions, i.e., compression and disruption. Their simulation, however, has the following limitations. (1) An aggregate contains as few as 40 particles. (2) They consider only one kind of structure for the initial aggregate; this is far from enough for statistical discussions. (3) Their simulation is limited to two-dimensional (2D) and head-on collisions; there would be differences in the collisional outcomes between 2D and three-dimensional (3D), and head-on and offset collision.

It is of course difficult to directly simulate collisions of large aggregates, say, of centimeter size, consisting of more than billions of submicron monomers. Therefore, a reasonable way is that we first perform simulation of collisions of aggregates consisting of $\lesssim 10^4$ particles and then extrapolate the results to larger sizes. For such an extrapolation, we have to clarify the dependence of the collisional outcomes on the number of particles composing aggregates, as well as the parameters relevant to the particle interactions.

In this paper, we focus on 2D simulations of head-on collisions of BCCAs as a first step of our study and test the recipe of Dominik & Tielens (1997). In a subsequent paper, we will carry out 3D simulations under various initial conditions (e.g., head-on and offset collisions). In § 2, we describe a particle interaction model used in our simulation. This model is similar to that used in Dominik & Tielens (1997). We introduce the potential energies that give the particle interactions to ensure conservation of total energy in the case of no energy dissipation. At aggregate

collisions, the impact kinetic energy is the source for transformation, compression, or breakup of the aggregates. Artificial changes in the total energy must be avoided in the numerical simulations. Using these potentials, we can derive consistent formulae of the forces and the torques exerted on the particles in contact. We summarize the recipe of Dominik & Tielens (1997) in § 3. In § 4 we describe the numerical procedure of our simulation together with the initial conditions and the parameters used in our simulation. We show the results of our simulations and discuss the results in § 5. In the results, we mainly focus on compression and disruption of aggregates. We examine aggregate compression quantitatively by measuring the gyration radii and the number of contacts of the resulting aggregates. A summary is given in § 6.

2. PARTICLE INTERACTION MODEL

In our numerical simulations, aggregates consist of a number of spherical particles with radius of $0.1 \mu\text{m}$ made of quartz or ice. We calculate the motion of individual particles by solving the equation of motion for each particle (Dominik & Tielens 1997). Each particle is an elastic sphere having a surface energy. When two particles are in contact, their elastic behavior produces a repulsive force between them, and the surface energy causes an attractive force. The repulsive and the attractive forces are formulated by Johnson et al. (1971). According to their theory (the so-called JKR theory), these forces depend on the distance between the centers of the two particles in contact (see also Johnson 1987). Furthermore, when the particles in contact slide, roll, or twist with respect to each other, forces against motions are exerted on the particles. These forces are formulated by Dominik & Tielens (1995, 1996).

In this section, we describe details of our particle interaction model. Although this study focuses on 2D simulation, we formulate a model of 3D interactions so as to be applicable to extended studies. Our formulation is similar to that described in Dominik & Tielens (1997). We use the contact pointers similar to those introduced in Dominik & Nübold (2002). In our model, we newly introduce potential energies for the particle interactions, which enable us to readily develop the formulation of the particle interaction.

2.1. Repulsive and Attractive Forces in the Normal Direction

For later use, we summarize the JKR theory (Johnson et al. 1971; Johnson 1987). We consider two particles 1 and 2 of radii r_1 and r_2 in contact with each other. The position vectors of the two particles' centers are \mathbf{x}_1 and \mathbf{x}_2 , respectively. Their Young's moduli are denoted by E_1 and E_2 , Poisson's ratios by ν_1 and ν_2 , and shear moduli by G_1 and G_2 . The surface energy per unit contact area between the two particles is γ . We use the same values for these quantities as those used in Dominik & Tielens (1997). Table 2 summarizes the parameter values.

Two particles in contact make a contact surface area that is approximately given by a flat disk of radius a . At an equilibrium state where the repulsive force is balanced with the attractive force, a is equal to the equilibrium radius a_0 given by

$$a_0 = \left(\frac{9\pi\gamma R^2}{E^*} \right)^{1/3}, \quad (1)$$

where the reduced particle radius R and the reduced Young's modulus E^* are given by

$$\frac{1}{R} = \frac{1}{r_1} + \frac{1}{r_2}, \quad \frac{1}{E^*} = \frac{1 - \nu_1^2}{E_1} + \frac{1 - \nu_2^2}{E_2}, \quad (2)$$

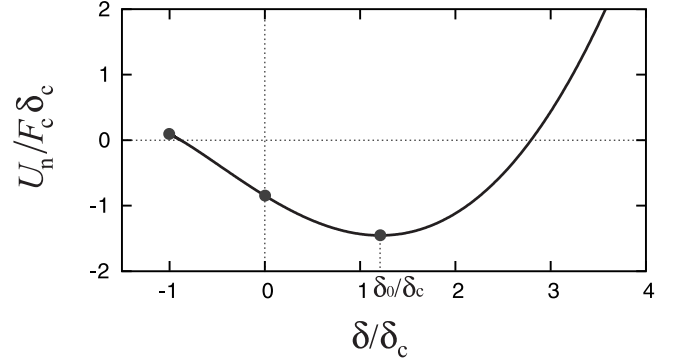


FIG. 1.—Potential U_n as a function of compression length δ .

respectively. The compression length between two contact particles, δ , is defined by

$$\delta = r_1 + r_2 - |\mathbf{x}_1 - \mathbf{x}_2|. \quad (3)$$

The contact disk radius a is related to the compression length δ as

$$\frac{\delta}{\delta_0} = 3 \left(\frac{a}{a_0} \right)^2 - 2 \left(\frac{a}{a_0} \right)^{1/2}, \quad (4)$$

where $\delta_0 = a_0^2/(3R)$ is the equilibrium compression length when $a = a_0$.

The force acting between two contact particles, F , is given by

$$\frac{F}{F_c} = 4 \left[\left(\frac{a}{a_0} \right)^3 - \left(\frac{a}{a_0} \right)^{3/2} \right], \quad (5)$$

where $F_c = 3\pi\gamma R$ is the maximum force needed to separate the two contact particles. In the right-hand side of equation (5), the first term indicates the repulsive force and the second one the attractive force. At the moment of separation, δ equals $-\delta_c$, where $\delta_c = (9/16)^{1/3} \delta_0$.

The potential energy for normal motion of the two contact particles, U_n , which is the sum of the elastic and the surface energies, is given by

$$\frac{U_n}{F_c \delta_c} = 4 \times 6^{1/3} \left[\frac{4}{5} \left(\frac{a}{a_0} \right)^5 - \frac{4}{3} \left(\frac{a}{a_0} \right)^{7/2} + \frac{1}{3} \left(\frac{a}{a_0} \right)^2 \right]. \quad (6)$$

The force F and the potential energy U_n may be expressed as functions of δ with the use of equation (4). Figure 1 shows U_n with respect to δ . One should note that the potential curve in the region of $\delta < 0$ is meaningful only when the two particles are in contact, whereas before contact, $U_n = 0$ for $\delta < 0$. It is useful to express the normal component of the force acting on the particle 1 due to the contact with the particle 2 with the use of the potential U_n as

$$\mathbf{F}_{n,1} = - \frac{\partial U_n}{\partial \mathbf{x}_1} = \frac{\partial U_n}{\partial \delta} \frac{\mathbf{x}_1 - \mathbf{x}_2}{|\mathbf{x}_1 - \mathbf{x}_2|}, \quad (7)$$

where we used equation (3). Note that the absolute value of $\mathbf{F}_{n,1}$ agrees with F given by equation (5).

Energy dissipates as elastic waves (Chokshi et al. 1993) at the moments of contact and separation of particles because of step

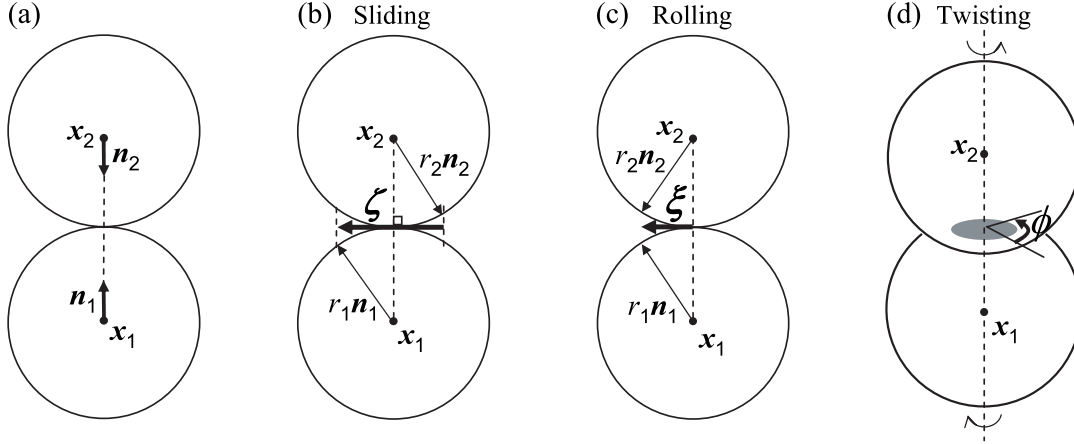


FIG. 2.—Schematic illustrations of (a) the beginning of contact, (b) sliding, (c) rolling, and (d) twisting. The contact pointers for the particles 1 and 2 are represented by \mathbf{n}_1 and \mathbf{n}_2 , respectively. Sliding and rolling motions are indicated by the motions of \mathbf{n}_1 and \mathbf{n}_2 . Displacements due to the motions (b), (c), and (d) are denoted by ζ , ξ , and ϕ , respectively.

discontinuities in the potential U_n . At contact, U_n jumps from zero to $U_n(\delta = 0) (\simeq -0.847F_c\delta_c)$, and at separation $\delta = -\delta_c$, U_n jumps from $U_n(\delta = -\delta_c) (\simeq 0.089F_c\delta_c)$ to zero.

2.2. Resistances to Tangential Motions

The tangential motion of two particles in contact can be divided into sliding, rolling, and twisting. The displacements corresponding to these motions are expressed by the rotation of the two particles (see Fig. 2). In this subsection, we describe the displacements and the resistances against these displacements. When the displacements of the tangential motions are all small enough, no energy is dissipated in the tangential motions. Such an elastic regime is described in §§ 2.2.1–2.2.4. We also describe in § 2.2.5 the inelastic regime where some of the displacements are large enough. As for the forces and the torques, we use the results of Dominik & Tielens (1995, 1996, 1997) and the method of Dominik & Nübold (2002) but modify their method so as to ensure the conservation of the total mechanical energy in the case of no dissipation.

2.2.1. Sliding Motion

In the description of sliding and rolling motions between two particles, it is useful to introduce “contact pointers” \mathbf{n}_1 and \mathbf{n}_2 (Dominik & Nübold 2002), which are unit vectors originating from the center of each particle and initially oriented to the contact point (see Fig. 2a). After the instance of contact, rotation of each particle changes the directions of \mathbf{n}_1 and \mathbf{n}_2 . Using the contact pointers, we define the sliding displacement ζ as follows. Let ζ_0 be a vector given by

$$\zeta_0 = r_1\mathbf{n}_1 - r_2\mathbf{n}_2 + (r_1 + r_2)\mathbf{n}_c, \quad (8)$$

where another unit vector \mathbf{n}_c is defined by

$$\mathbf{n}_c = \frac{\mathbf{x}_1 - \mathbf{x}_2}{|\mathbf{x}_1 - \mathbf{x}_2|}. \quad (9)$$

The vector ζ_0 is not perpendicular to the vector $\mathbf{x}_1 - \mathbf{x}_2$; namely, ζ_0 is not tangential. The sliding displacement ζ , the component of ζ_0 perpendicular to the vector \mathbf{n}_c (see Fig. 2b), is given by

$$\zeta = \zeta_0 - (\zeta_0 \cdot \mathbf{n}_c)\mathbf{n}_c. \quad (10)$$

With the use of ζ , the potential energy stored by the sliding motion is written as

$$U_s = \frac{1}{2}k_s|\zeta|^2, \quad (11)$$

where the spring constant k_s is given (Johnson 1987) by

$$k_s = 8a_0G^*, \quad (12)$$

with

$$\frac{1}{G^*} = \frac{2 - \nu_1}{G_1} + \frac{2 - \nu_2}{G_2}. \quad (13)$$

The spring constant k_s leads to the force given in equation (14), which agrees with that of Johnson (1987). Exactly speaking, Johnson (1987) used a instead of a_0 . We use a_0 in order to make U_s independent of the compression length δ . This independence is necessary for the total energy conservation if we use the JKR theory for the normal component of interaction.

By using the sliding potential U_s , we can obtain the force $\mathbf{F}_{s,1}$ acting on the particle 1 due to sliding motion between the particles 1 and 2 as

$$\mathbf{F}_{s,1} = -\frac{\partial U_s}{\partial \mathbf{x}_1} = -k_s\zeta \frac{r_1 + r_2 - \zeta_0 \cdot \mathbf{n}_c}{|\mathbf{x}_1 - \mathbf{x}_2|}. \quad (14)$$

The factor $(r_1 + r_2 - \zeta_0 \cdot \mathbf{n}_c)/|\mathbf{x}_1 - \mathbf{x}_2|$ is essential for energy conservation and is ~ 1 when the displacement is small. A torque acting on the particle 1 due to the potential U_s is given by

$$\mathbf{M}_{s,1} = -\frac{\partial U_s}{\partial \boldsymbol{\theta}_1}, \quad (15)$$

where $\boldsymbol{\theta}_1$ is the rotational angle vector of the particle 1. For further transformation, we use the infinitesimal change of the contact pointer \mathbf{n}_1 given by $\delta\mathbf{n}_1 = \delta\boldsymbol{\theta}_1 \times \mathbf{n}_1$. The change in the potential, δU , due to $\delta\mathbf{n}_1$ is written by

$$\delta U \equiv \frac{\partial U}{\partial \mathbf{n}_1} \cdot \delta\mathbf{n}_1 = \left(\mathbf{n}_1 \times \frac{\partial U}{\partial \mathbf{n}_1} \right) \cdot \delta\boldsymbol{\theta}_1. \quad (16)$$

Using this relation, equation (15) is expressed by

$$\mathbf{M}_{s,1} = -\mathbf{n}_1 \times \frac{\partial U_s}{\partial \mathbf{n}_1} = -r_1 k_s \mathbf{n}_1 \times \boldsymbol{\zeta}. \quad (17)$$

We get the force $\mathbf{F}_{s,2}$ and the torque $\mathbf{M}_{s,2}$ on the particle 2 due to the sliding by interchanging the suffixes 1 and 2 and by replacing $\boldsymbol{\zeta}$ by $-\boldsymbol{\zeta}$ (see eqs. [14] and [17]).

It is readily seen that the forces and the torques derived from the potential U_s satisfy

$$\mathbf{F}_{s,1} + \mathbf{F}_{s,2} = 0 \quad (18)$$

and

$$\mathbf{M}_{s,1} + \mathbf{M}_{s,2} + \mathbf{F}_{s,1} \times \frac{\mathbf{x}_1 - \mathbf{x}_2}{2} + \mathbf{F}_{s,2} \times \frac{\mathbf{x}_2 - \mathbf{x}_1}{2} = 0, \quad (19)$$

confirming the conservations of the momenta and the angular momenta.

2.2.2. Rolling Motion

The rolling displacement $\boldsymbol{\xi}$ is defined by

$$\boldsymbol{\xi} = R(\mathbf{n}_1 + \mathbf{n}_2), \quad (20)$$

where we recall that R is the reduced particle radius given by equation (2). The potential energy for the displacement $\boldsymbol{\xi}$ is given by

$$U_r = \frac{1}{2} k_r |\boldsymbol{\xi}|^2, \quad (21)$$

where the spring constant k_r in the rolling motion is defined by

$$k_r = \frac{4F_c}{R}. \quad (22)$$

Since $\partial U_r / \partial \mathbf{x}_i = 0$, the potential U_r exerts no forces on the particles but torque on the particle 1 given by

$$\mathbf{M}_{r,1} = -\mathbf{n}_1 \times \frac{\partial U_r}{\partial \mathbf{n}_1} = -R k_r \mathbf{n}_1 \times \boldsymbol{\xi}, \quad (23)$$

which agrees with that of Dominik & Tielens (1995). The torque $\mathbf{M}_{r,2}$ on the particle 2 is obtained in the same way. These torques satisfy $\mathbf{M}_{r,1} + \mathbf{M}_{r,2} = 0$, indicating the conservation of the angular momenta of the particles.

2.2.3. Twisting Motion

We define the twisting angular vector $\boldsymbol{\phi}$ (see Fig. 2d) by

$$\boldsymbol{\phi} = \mathbf{n}_c \int^t (\boldsymbol{\omega}_1 - \boldsymbol{\omega}_2) \cdot \mathbf{n}_c dt, \quad (24)$$

where $\boldsymbol{\omega}_1$ and $\boldsymbol{\omega}_2$ are the angular velocity vectors of the particles 1 and 2, respectively, and the time integration is done from the instant of contact. The potential energy stored at a twisting angle $\boldsymbol{\phi}$ is given by

$$U_t = \frac{1}{2} k_t |\boldsymbol{\phi}|^2, \quad (25)$$

where the spring constant k_t is given (Johnson 1987) by

$$k_t = \frac{16}{3} G a_0^3, \quad (26)$$

where $G = (1/G_1 + 1/G_2)^{-1}$ is the reduced shear modulus of the two particles. The torque acting on the particle 1 due to twisting is given by

$$\mathbf{M}_{t,1} = -\frac{\partial U_t}{\partial \boldsymbol{\phi}} = -k_t \boldsymbol{\phi}, \quad (27)$$

and the torque $\mathbf{M}_{t,2}$ on the particle 2 equals $-\mathbf{M}_{t,1}$.

2.2.4. Tracing of the Contact Pointers

We briefly explain the method of tracing the contact pointers \mathbf{n}_1 and \mathbf{n}_2 in a similar way to that of Dominik & Nübold (2002). Suppose that particles 1 and 2 begin to be in contact at time t_0 , when $\mathbf{n}_1(t_0) = -\mathbf{n}_c(t_0)$. For $t > t_0$, we trace the contact pointer by the rotational transformation of $\mathbf{n}_1(t_0)$ with the use of a matrix $A_1(t)$, which carries out the rotational transformation of vectors from the inertial coordinate system to the coordinates fixed to the particle 1 (i.e., rotating with the particle 1). At time t , the contact pointer in the coordinates rotating with the particle 1 is given by $\mathbf{n}'_1 = A_1(t)\mathbf{n}_1(t)$. The contact pointer does not change in the coordinates fixed to the particle 1, so the vector \mathbf{n}'_1 is constant. The constant vector \mathbf{n}'_1 is given by

$$\mathbf{n}'_1 = A_1(t_0)\mathbf{n}_1(t_0). \quad (28)$$

Using \mathbf{n}'_1 , we obtain $\mathbf{n}_1(t)$ as

$$\mathbf{n}_1(t) = A_1^{-1}(t)\mathbf{n}'_1. \quad (29)$$

The rotation matrix A is expressed by three Eulerian angles or Eulerian parameters (see, e.g., Goldstein 1950). We use Eulerian parameters because they are more tractable than Eulerian angles in numerical computations. A rotational transformation of the coordinates by an angle ψ around an axis whose direction is given by the unit vector $\hat{\psi}$ is characterized by the Eulerian parameters, e_0 and $\mathbf{e} = (e_1, e_2, e_3)$ given by

$$e_0 = \cos \frac{\psi}{2}, \quad \mathbf{e} = \hat{\psi} \sin \frac{\psi}{2}, \quad (30)$$

respectively, which satisfy the relation $e_0^2 + e_1^2 + e_2^2 + e_3^2 = 1$. By using the Eulerian parameters, the (i, j) component of the rotation matrix A_{ij} is given (Goldstein 1950) by

$$A_{ij} = (1 - 2e^2)\delta_{ij} + 2e_i e_j + 2e_0 \sum_{k=1}^3 \epsilon_{ijk} e_k, \quad (31)$$

where δ_{ij} is Kronecker's delta and ϵ_{ijk} is Levi-Civita's epsilon.

The Eulerian parameters are defined for each particle and change with time according to rotation of the particle. The time evolution of the Eulerian parameters is described by the following equations¹ (Goldstein 1950; Dominik & Nübold 2002):

$$\frac{de_0}{dt} = \frac{1}{2} \mathbf{e} \cdot \boldsymbol{\omega}, \quad (32)$$

$$\frac{d\mathbf{e}}{dt} = \frac{1}{2} (e_0 \boldsymbol{\omega} - \mathbf{e} \times \boldsymbol{\omega}), \quad (33)$$

where $\boldsymbol{\omega}$ is the angular velocity of the particle in the inertial coordinates. We take the coordinates fixed to the particle to match

¹ Note that the equations of e_0 and \mathbf{e} are usually expressed in terms of the angular velocity $\boldsymbol{\omega}'$ in the coordinates fixed to the particle, where $\boldsymbol{\omega}' = A\boldsymbol{\omega}$. Equations (32) and (33) can be readily derived from the usual expressions.

the inertial coordinates at $t = 0$. This gives the initial condition of the Eulerian parameters as

$$e_0(t = 0) = 1, \quad e(t = 0) = 0. \quad (34)$$

Integrating equations (32) and (33) with the initial conditions (34), we calculate the Eulerian parameters, the rotation matrix $A_1(t)$, and the contact pointer $\mathbf{n}_1(t)$ at any time t for each particle.

2.2.5. Inelastic Regimes in the Sliding, the Rolling, and the Twisting Motion

The resistances to sliding, rolling, and twisting described in §§ 2.2.1–2.2.4 are restricted in the elastic regime. When the displacements due to these motions become greater than the critical values, particle motions enter the inelastic regime accompanied by energy dissipation.

Our treatment of the motions in the inelastic regime is based on Dominik & Tielens (1997), but a noticeable difference is mentioned here. In their model, once the displacement in the elastic regime exceeds a critical value, the force or torque is reset to zero. In our model, the force or torque is kept to the value at the critical displacement, and the displacement does not increase any more (see Fig. 3). Furthermore, when the displacement begins to decrease, the motion is treated as elastic again. In this way, the force or torque is continuous at the critical displacement and ensures high accuracy of energy conservation in the numerical calculation.

Let us describe the critical displacement for each kind of motion according to Dominik & Tielens (1997). The frictional force originating in the steps (irregularities) on the surfaces is given by

$$F_{\text{fric}} = \frac{Ga_0^2}{2\pi}, \quad (35)$$

when the particles slide over the elastic limit. We assume $a = a_0$ in the expression of F_{fric} of Dominik & Tielens (1996, 1997) to guarantee the conservation of the total energy in the elastic motion. In fact, F_{fric} involves another force proportional to the contact area πa_0^2 due to intermolecular interaction between two particles through the contact (Dominik & Tielens 1996, 1997). This intermolecular force is negligible for quartz compared to that due to the surface steps but is comparable for ice or metal. In the latter case, one can include the intermolecular force by modifying G in equation (35) because both the force due to surface steps and the intermolecular force are proportional to the area πa_0^2 if an external force is ignored. In practice, the inelastic sliding does not play a role in the aggregate restructuring, which is mainly caused by rolling motion of the particles (Dominik & Tielens 1996, 1997). Equating the elastic force given by equation (14) to F_{fric} , we obtain the critical displacement of sliding

$$\zeta_{\text{crit}} = \frac{2 - \nu}{16\pi} a_0, \quad (36)$$

where we simplified the elastic force as $-k_s \zeta$.

Dominik & Tielens (1995) set the critical displacement of rolling to be $\xi_{\text{crit}} = 2 \text{ \AA}$, whereas the experiments by Heim et al. (1999) suggest that $\xi_{\text{crit}} \simeq 32 \text{ \AA}$ for $1.8 \text{ }\mu\text{m}$ sized SiO_2 particles. We set ξ_{crit} to be a parameter in our simulation because of the uncertainty of the ξ_{crit} values for quartz or ice particles. The torque for twisting in the inelastic regime is given by

$$M_{t, \text{fric}} = \frac{Ga_0^3}{3\pi}, \quad (37)$$

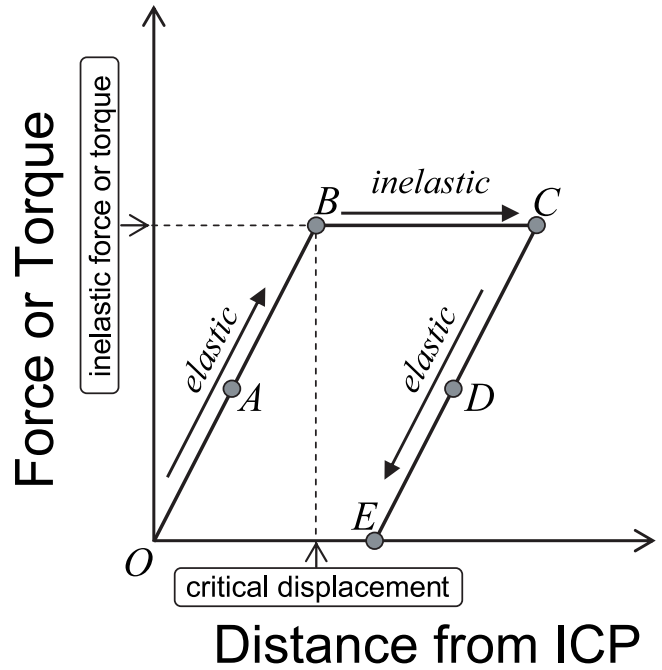


FIG. 3.—Force or torque as a function of distance measured from an initial contact point (ICP). When the displacement is small (at point A), the force or torque is proportional to the displacement as given by the elastic formula. Once the displacement becomes greater than the critical value (B), the force or torque is given by the inelastic formula and kept constant until the reverse of motion (C). After the reverse at C, the displacement and the force (or the torque) return to the elastic regime (D). The elastic equilibrium position originally at O is moved to E by the inelastic motion.

where we take the torque resulting from steps in the expression of Dominik & Tielens (1996). Using equations (27) and (37), a critical angle for twisting is given by

$$\phi_{\text{crit}} = \frac{1}{16\pi} \simeq 1.1^\circ. \quad (38)$$

When the sliding displacement $|\zeta|$ exceeds the elastic limit ζ_{crit} at a time step, the particle motion enters the inelastic regime and energy dissipation occurs. The energy dissipation by the inelastic sliding at this time step is given by

$$\Delta E_{\text{dis}, s} = k_s \zeta_{\text{crit}} (|\zeta| - \zeta_{\text{crit}}). \quad (39)$$

Before the next time step, we restore the sliding displacement $|\zeta|$ to ζ_{crit} . The energy dissipation $\Delta E_{\text{dis}, s}$ for each time step is accumulated during the period of inelastic motion. In the same way, the energy dissipations $\Delta E_{\text{dis}, r}$ and $\Delta E_{\text{dis}, t}$ due to rolling and twisting are, respectively, given by

$$\Delta E_{\text{dis}, r} = k_r \xi_{\text{crit}} (|\xi| - \xi_{\text{crit}}), \quad (40)$$

$$\Delta E_{\text{dis}, t} = k_t \phi_{\text{crit}} (|\phi| - \phi_{\text{crit}}). \quad (41)$$

We need to modify the contact pointers to express the restoring of the displacements to their elastic limits. Suppose that inelastic sliding occurs at time $t = t_{ie}$. For the increment of the displacement from the critical position, $\Delta \zeta = \zeta(1 - \zeta_{\text{crit}}/|\zeta|)$, the contact pointers \mathbf{n}_1 and \mathbf{n}_2 at $t = t_{ie}$ should be corrected as

$$\mathbf{n}_1^c(t_{ie}) = \mathbf{n}_1(t_{ie}) - \frac{\Delta \zeta}{2r_1} \alpha, \quad \mathbf{n}_2^c(t_{ie}) = \mathbf{n}_2(t_{ie}) - \frac{\Delta \zeta}{2r_2} \alpha, \quad (42)$$

where α is a correction factor to assure the direction of the contact pointer after normalization (see the Appendix for details). Normalizing \mathbf{n}_1^c , we obtain the new contact pointer $\mathbf{n}_1^{\text{new}}(t_{ic})$. We renew the constant vector \mathbf{n}_1' by operating the rotation matrix $A_1(t_{ic})$ to $\mathbf{n}_1^{\text{new}}(t_{ic})$:

$$\mathbf{n}_1' = A_1(t_{ic})\mathbf{n}_1^{\text{new}}(t_{ic}). \quad (43)$$

The contact pointer at $t > t_{ic}$ is calculated by equation (29) with the use of newly obtained \mathbf{n}_1' . For inelastic rolling, we modify \mathbf{n}_1' and \mathbf{n}_2' in a similar way as the inelastic sliding.

3. DT RECIPE

For later discussion, we summarize the results obtained by the numerical simulation of Dominik & Tielens (1997). They formulated a recipe, which we call the DT recipe, for the dependence of collisional outcomes on impact energy E_{imp} . Table 1 summarizes the DT recipe, which is expressed in terms of three parameters E_{roll} , E_{break} , and n_k . The energy necessary to roll a particle by 90° around its contact point is represented by E_{roll} and is given by

$$E_{\text{roll}} = k_r \xi_{\text{crit}} \pi R = 12\pi^2 \gamma R \xi_{\text{crit}} \quad (44)$$

in our model. The rolling torque in our model is kept at its maximum value when the inelastic rolling occurs, while that in Dominik & Tielens (1997) is reset to 0. Therefore, the amount of the energy dissipated by inelastic rolling (i.e., E_{roll}) in our model is twice that of Dominik & Tielens (1997). The energy E_{break} is the energy necessary to break completely a contact in the equilibrium position. Using the potential energy given by equation (6), E_{break} is expressed by

$$E_{\text{break}} = U_n(\delta_c) - U_n(\delta_0) \simeq 1.54 F_c \delta_c. \quad (45)$$

In Table 1, n_k is the total number of contacts in aggregates before impact.

According to Table 1, aggregates begin to be visibly restructured in a collision by rolling at impact energy of $\sim 5E_{\text{roll}}$. When the impact energy is nearly equal to $n_k E_{\text{roll}}$, which is the least energy to roll all contact points, aggregates are compressed to a maximum extent. Aggregates impacted with impact energy of $3n_k E_{\text{break}}$, i.e., 3 times the energy to break all contacts, begin to be disrupted, ejecting a few fragment particles. If the impact energy is greater than $10n_k E_{\text{break}}$, catastrophic disruption occurs. Here, catastrophic disruption means that the number of particles in the largest cluster after impact becomes less than the half the total. These energy criteria for the maximum compression and the disruption may be scaled by using n_k , which is nearly equal to the total number of particles in aggregates. This scaling suggests that the collision outcomes are determined only by the impact velocity, irrespective of the aggregate size (i.e., the number of particles composing the aggregates).

The DT recipe seems to explain the experimental results of 3D small aggregate (~ 60 particles) collisions by Blum & Wurm (2000). However, the recipe is confirmed by the numerical simulations under limited conditions such as 2D head-on collisions, small aggregates consisting of 40 particles, and one type of initial structure of the aggregates. Furthermore, their criteria are based on visual observation of the numerical outcomes. We shall examine quantitatively whether or not the DT recipe holds under wide ranges of conditions of aggregate collisions by carrying out numerical simulations for aggregates composed of a large number of particles and under various initial conditions. We limit the

TABLE 1
RECIPE FOR AGGREGATE COLLISION PROPOSED
BY DOMINIK & TIELENS (1997)

Energy	Collisional Outcome
$E_{\text{imp}} \approx 5E_{\text{roll}}$	First visible restructuring
$E_{\text{imp}} \approx n_k E_{\text{roll}}$	Maximum compression
$E_{\text{imp}} \approx 3n_k E_{\text{break}}$	Loss of one particle
$E_{\text{imp}} > 10n_k E_{\text{break}}$	Catastrophic disruption

simulation to 2D in the present paper to compare our results with those of Dominik & Tielens (1997).

4. NUMERICAL PROCEDURE

The equations of motion for translational and rotational motions of the i th particle in aggregates are given by

$$m_i \frac{d\mathbf{v}_i}{dt} = \sum_j (\mathbf{F}_{n,ij} + \mathbf{F}_{s,ij}), \quad (46)$$

$$I_i \frac{d\boldsymbol{\omega}_i}{dt} = \sum_j (\mathbf{M}_{s,ij} + \mathbf{M}_{r,ij} + \mathbf{M}_{t,ij}), \quad (47)$$

where m_i , I_i , \mathbf{v}_i , and $\boldsymbol{\omega}_i$ are the mass, moment of inertia, velocity, and angular velocity of the particle i , respectively. The forces and torques on the particle i exerted by the particle j are denoted by $\mathbf{F}_{n,ij}$, $\mathbf{F}_{s,ij}$, $\mathbf{M}_{s,ij}$, $\mathbf{M}_{r,ij}$, and $\mathbf{M}_{t,ij}$, which are given in § 2. The summations of the forces and the torques on the right-hand sides of both equations are taken for all particles in contact with the particle i . These equations of motion and the evolutionary equations of Eulerian parameters given by equations (32) and (33) for each particle are integrated using the leapfrog method in our simulation. This is a second-order symplectic integrator and realizes a good accuracy of energy conservation, as is shown later. At contact and separation of particles, we modify the positions and velocities of the particles by a linear interpolation to fit them to the true values.

We need to find pairs of particles in contact to calculate particle interaction. It costs much time to calculate the distances for all pairs of particles. To save computation time, we introduce a spatial cell division method (e.g., Wada et al. 2006), in which we divide the computational space into cubic cells of the same size and make a list of cells in which particles are packed. With using this method, we only search the cells around the particle i when particles around the particle i need to be detected, and calculate the distances between the particle i and others in those cells. The size of the cells is set to $1.15r_1$ in our simulation.

The characteristic force, length, and mass in our simulation are F_c , δ_c , and m_1 , respectively. The characteristic velocity v_0 derived from them is

$$v_0 = \sqrt{\frac{F_c \delta_c}{m_1}}. \quad (48)$$

Using the material parameters listed in Table 2, we have $v_0 = 0.308 \text{ m s}^{-1}$ for quartz and $v_0 = 3.08 \text{ m s}^{-1}$ for ice. In our simulation, the collisional velocity is varied from $0.14v_0$ to $18v_0$. The characteristic time t_c is

$$t_c = \frac{\delta_c}{v_0} = \sqrt{\frac{m_1 \delta_c}{F_c}}. \quad (49)$$

TABLE 2
MATERIAL PARAMETERS

Material	γ (mJ m ⁻²)	E (GPa)	ν	Density (kg m ⁻³)
Quartz.....	25	54	0.17	2600
Ice.....	100	7	0.25	1000

The time step is set to $0.014t_c$ in almost all of our simulation, which makes the relative error in the energy conservation less than 10^{-4} . To save computation time for the collisions of large aggregates composed of 2048 particles, the time step is set up to $0.112t_c$. Even in these cases, the relative error is less than 10^{-3} .

We take quartz and ice as grain materials (see Table 2). Their parameter values used for these materials are the same as used in Dominik & Tielens (1997) except for the surface energy of ice (Israelachvili 1992). According to Chokshi et al. (1993) and Dominik & Tielens (1997), the stickiness of quartz is the weakest among quartz, polystyrene, graphite, iron, and ice, and that of ice is the strongest. The critical rolling displacement ξ_{crit} is another parameter. We take $\xi_{\text{crit}} = 2$ and 30 \AA (Dominik & Tielens 1995; Heim et al. 1999). We investigate the four cases given in Table 3.

As the initial condition, we prepare 2D BCCAs because the structure of dust in the early stage of its growth is expected to be BCCA. The number of particles composing the initial aggregates is set to be 8, 32, 128, 512, or 2048 (see Fig. 4). These BCCAs are produced by random head-on sticking of two identical clusters successively. Head-on means that the approaching direction is parallel to the line connecting the centers of mass of two aggregates. By rotating the aggregates randomly in producing the aggregates, we prepare three types of BCCAs consisting of the same number of particles for a statistical study of the numerical results. The number of contacts in the aggregates produced here is given by $n_k = N_{\text{total}} - 2$ before impact, where N_{total} is the total number of particles in each simulation. The aggregates are impacted by head-on collisions. The aggregates consisting of 128 particles are used to investigate the influence of the material parameters shown in Table 3. For the aggregates of the other sizes, ξ_{crit} is fixed to 2 \AA to see the dependence of the collisional outcomes on the aggregate size.

5. RESULTS AND DISCUSSION

5.1. Examples of Collisional Outcomes

Typical examples of collisional outcomes for various impact velocities are shown in Figure 5. We simulate the aggregate collisions in the center-of-mass system, where the impact energy E_{imp} is given by $E_{\text{imp}} = (1/2)N_{\text{total}}m_1(v_{\text{imp}}/2)^2$, with v_{imp} being the relative impact velocity. The initial structure used in these example cases is the same BCCA composed of 128 quartz particles shown in Figure 4. We take $\xi_{\text{crit}} = 2 \text{ \AA}$ here. When the

TABLE 3
PARAMETERS AND CHARACTERISTIC ENERGIES

Material	ξ_{crit} (\AA)	$E_{\text{roll}}/(F_c\delta_c)$	$E_{\text{break}}/(F_c\delta_c)$	$E_{\text{roll}}/E_{\text{break}}$
Quartz.....	2	28.7	1.54	18.6
Quartz.....	30	430	1.54	279
Ice.....	2	2.98	1.54	1.94
Ice.....	30	44.8	1.54	29.1

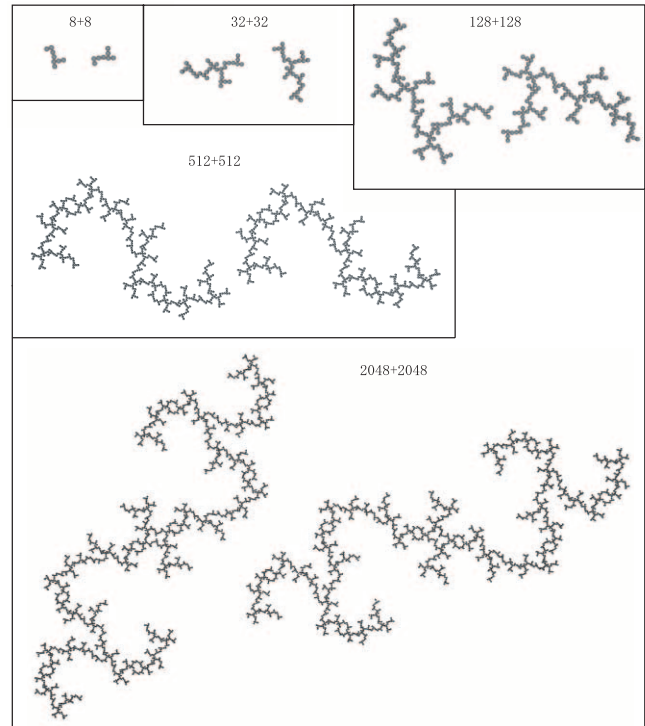


FIG. 4.—Examples of initial BCCAs. These aggregates collide with each other horizontally. Each aggregate consists of 8, 32, 128, 512, or 2048 identical particles.

impact velocity v_{imp} is low enough, the aggregates just hit and stick without any clear restructuring. With increasing v_{imp} , we see clearly that the aggregates after collision are restructured by rolling motion at several contact points and are consequently compressed (Fig. 5a). Figure 5b shows an aggregate compressed to almost its maximum extent. In Figure 5c, a fraction of the particles are lost from the resulting aggregate cluster. Considerable disruption occurs at a larger impact velocity (Fig. 5d).

Temporal changes in various kinds of energy in the case of Figure 5b are shown in Figure 6. The top panel of Figure 6

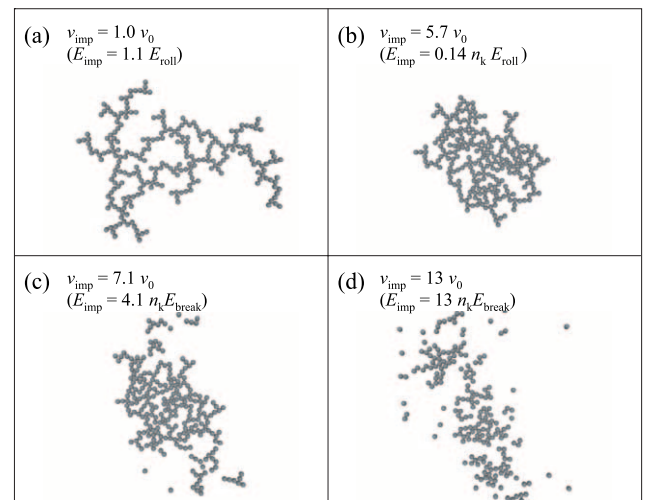


FIG. 5.—Examples of collisional outcomes for various impact velocities v_{imp} . Each case results in (a) visible restructuring, (b) maximum compression, (c) loss of a fraction of particles, or (d) catastrophic disruption. In all cases shown here, the initial aggregate consists of 128 quartz particles with $\xi_{\text{crit}} = 2 \text{ \AA}$, as shown in Fig. 4. See text for v_0 , E_{roll} , E_{break} , and n_k .

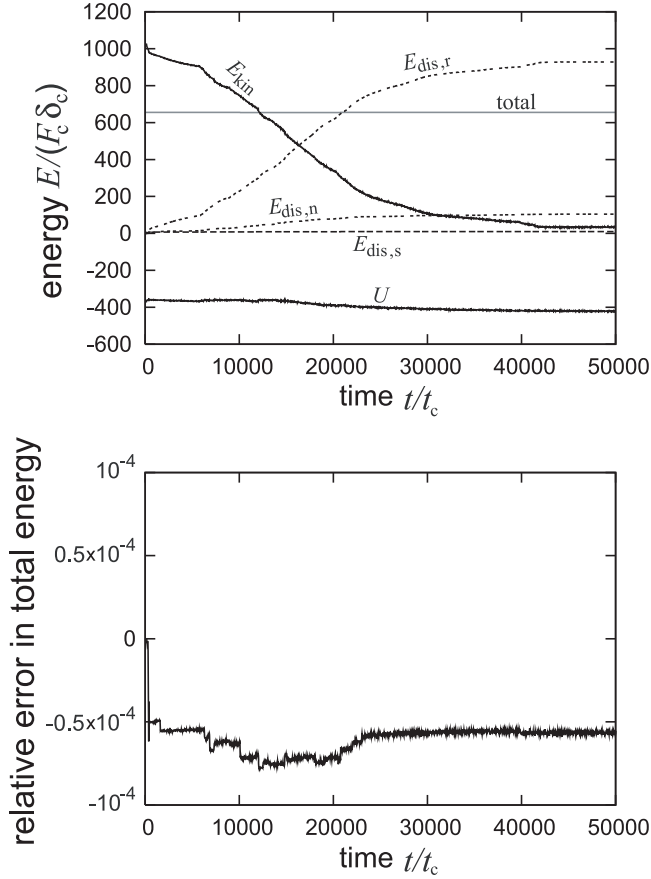


FIG. 6.—*Top*: Temporal changes in various kinds of energy at the collision shown in Fig. 5b. The kinetic energy (the sum of translational and rotational ones) is represented by E_{kin} , the total potential energy by U , and the amounts of energies dissipated in the motion of the normal direction by $E_{\text{dis},n}$, sliding motion by $E_{\text{dis},s}$, and rolling motion by $E_{\text{dis},r}$. The total energy including dissipated energies is represented by “total.” *Bottom*: Relative error in the total energy at the same collision.

indicates that almost all of the initial kinetic energy is dissipated by rolling motion. This is in agreement with the discussion by Dominik & Tielens (1997), who claim that the energy dissipation by rolling is much easier than that by sliding. We also see a slight increase in $E_{\text{dis},n}$ and a decrease in the total potential energy U owing to the increase of the number of contacts, indicating compaction of the aggregates at the collision.

The bottom panel of Figure 6 shows that the relative error in the total energy is less than 10^{-4} , indicating a good accuracy of the energy conservation in our simulation owing to the leapfrog integrator. The largest error arises at the moment of contact and separation of particles.

5.2. Gyration Radius

The gyration radius r_g of an aggregate is defined by

$$r_g = \sqrt{\frac{1}{N} \sum_i (\mathbf{x}_i - \mathbf{x}_M)^2}, \quad (50)$$

where \mathbf{x}_i is the position vector of particle i , \mathbf{x}_M is that of the center of mass of the aggregate, and N is the number of particles in the aggregate. The gyration radius is used as a measure for the change of aggregate size due to restructuring or compression. Figure 7a shows the gyration radius of the aggregate obtained by collisions of aggregates composed of 128 particles as a function of the impact energy normalized by $n_k E_{\text{roll}}$. When the aggregate is disrupted, the gyration radius is measured for the largest cluster. In this figure, the gyration radius is normalized by $r_1 N_{\text{large}}^{1/2}$, where N_{large} is the number of particles in the largest cluster. In 2D geometry, $r_1 N_{\text{large}}^{1/2}$ measures the size of a compact circle whose area is equal to that of the aggregate. For each parameter set, three curves are drawn, representing the different initial structures of aggregates. Figure 7a shows that the gyration radius decreases with increasing the impact energy at $E_{\text{imp}} \gtrsim 0.1 E_{\text{roll}}$, irrespective of the material parameters and the initial conditions. In the region

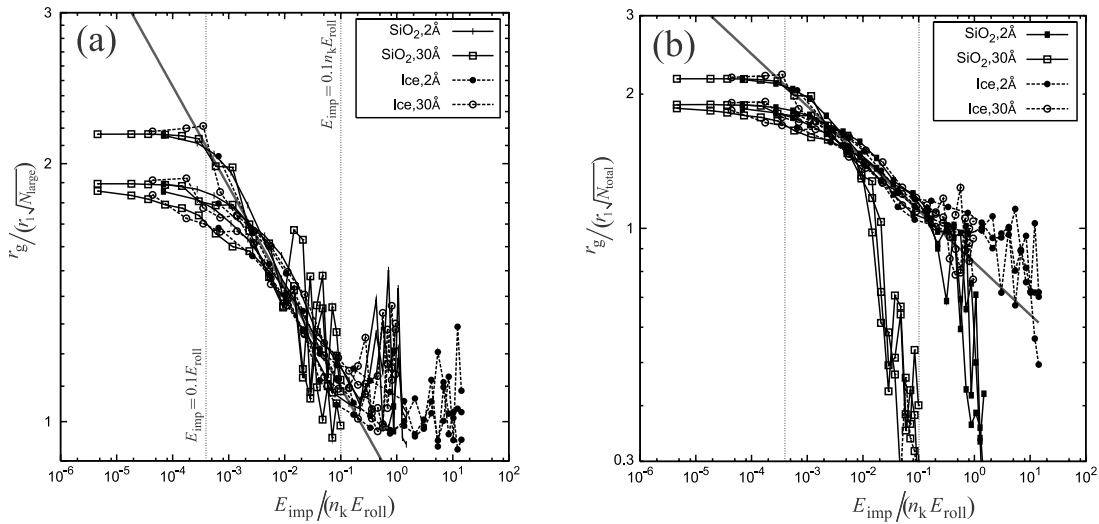


FIG. 7.—Gyration radius of the largest cluster, r_g , as a function of the impact energy E_{imp} . The vertical axes are $r_g/(r_1 N_{\text{large}}^{1/2})$ in (a) and $r_g/(r_1 N_{\text{total}}^{1/2})$ in (b). Each symbol corresponds to each parameter set: quartz with $\xi_{\text{crit}} = 2 \text{ \AA}$ (filled squares), quartz with $\xi_{\text{crit}} = 30 \text{ \AA}$ (open squares), ice with $\xi_{\text{crit}} = 2 \text{ \AA}$ (filled circles), and ice with $\xi_{\text{crit}} = 30 \text{ \AA}$ (open circles). Data plotted in this figure are all results of collisions of aggregates consisting of 128 particles. There are three types of initial aggregate structure for each parameter set. The dotted vertical lines indicate the impact energies equal to $0.1 E_{\text{roll}}$ and $0.1 n_k E_{\text{roll}}$. A fitting line (gray line) is drawn by using the data in the region of $E_{\text{roll}} < E_{\text{imp}} < 0.1 n_k E_{\text{roll}}$ and is expressed by $r_g/(r_1 N_{\text{large}}^{1/2}) = 0.84 [E_{\text{imp}}/(n_k E_{\text{roll}})]^{-0.12}$.

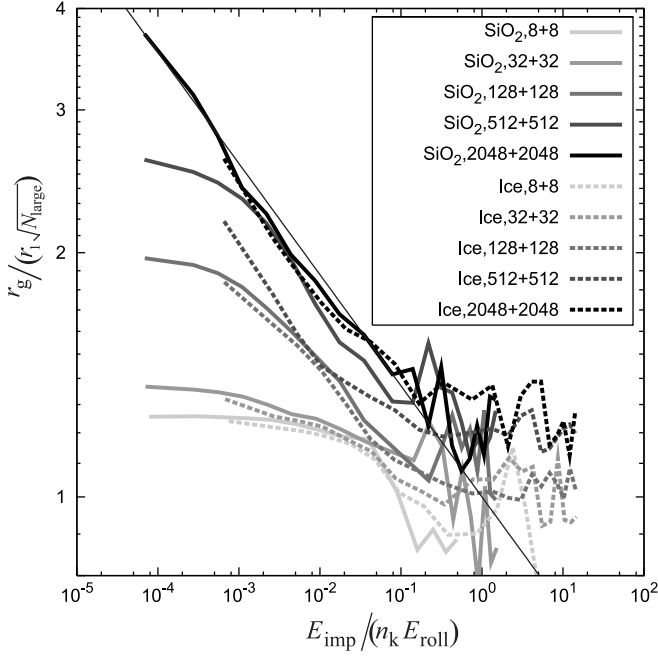


FIG. 8.— Same as Fig. 7a, but for aggregates with different sizes. For all cases, we take $\xi_{\text{crit}} = 2$ Å and average the outputs in three different initial aggregates produced by random numbers. Solid and dashed curves indicate the outcomes for quartz and ice aggregates, respectively. The gray scale for each curve corresponds to the number of particles (8, 32, 128, 512, and 2048) of the aggregate before impact. The thin line represents the relation $r_g / (r_1 N_{\text{large}}^{1/2}) = [E_{\text{imp}} / (n_k E_{\text{roll}})]^{-0.137}$.

of $E_{\text{roll}} < E_{\text{imp}} < 0.1 n_k E_{\text{roll}}$, the numerical results can be fitted by

$$\frac{r_g}{r_1 \sqrt{N_{\text{large}}}} = 0.84 \left(\frac{E_{\text{imp}}}{n_k E_{\text{roll}}} \right)^{-0.12}. \quad (51)$$

For $E_{\text{imp}} \gtrsim n_k E_{\text{roll}}$, the gyration radius stays at the lower limit of $\sim r_1 N_{\text{large}}^{1/2}$, indicating that compression of the aggregate through rolling is almost completed at $E_{\text{imp}} \sim n_k E_{\text{roll}}$. This agrees with the criterion of the maximum compression in the DT recipe, although an impact energy that is somewhat lower than $n_k E_{\text{roll}}$ may be enough for the maximum compression.

For $E_{\text{imp}} \gtrsim 0.1 n_k E_{\text{roll}}$, the gyration radius becomes scattered for each parameter set in Figure 7a. This scattering in r_g is caused by disruption of the aggregate, as is seen from Figure 7b, in which the gyration radius is normalized by using the total number of particles N_{total} . Figure 7b shows that $r_g / (r_1 N_{\text{total}}^{1/2})$ for each parameter set decreases suddenly from around unity at the impact energy where the gyration radius becomes scattered in Figure 7a. This indicates that aggregates are disrupted in such a range of impact energies. As is clearly seen in Figure 7, the impact-energy range for the aggregate disruption depends on the parameter values given in Table 3. This indicates that the disruption process cannot be scaled by $n_k E_{\text{roll}}$ alone. Details of the disruption process will be discussed later.

Figure 8 plots the change in $r_g / (r_1 N_{\text{large}}^{1/2})$ with varying the number of particles in the aggregates to show the dependence of the compression degree on the aggregate size N_{total} . The slope of the gyration radius as a function of E_{imp} is steeper for large aggregates than that for small aggregates. This is only because the filling factor of small BCCAs is higher than that of large BCCAs in general; in other words, small BCCAs are already rather compact before being compressed, so the change in the gyration

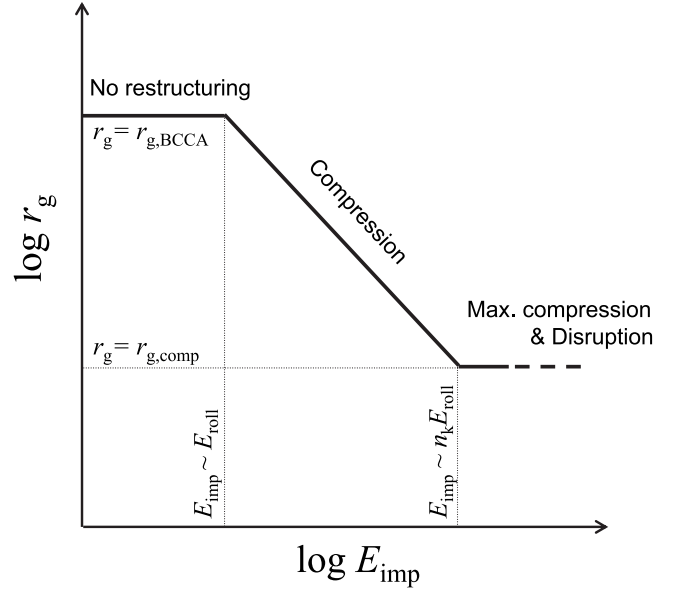


FIG. 9.— Change in gyration radius r_g as a function of impact energy E_{imp} . BCCAs with $r_g = r_{g,\text{BCCA}}$ start to be compressed at $E_{\text{imp}} \sim E_{\text{roll}}$, and their compression ends at $E_{\text{imp}} \sim n_k E_{\text{roll}}$.

radius for small aggregates is small even if they are compressed to the maximum.

In Figure 8 the slope of the lines for $E_{\text{roll}} \lesssim E_{\text{imp}} \lesssim 0.1 n_k E_{\text{roll}}$ seems to have a constant value (i.e., $d \log r_g / d \log E_{\text{imp}} \simeq -0.14$) for sufficiently large N_{total} . This slope is explained as follows (see also Fig. 9). The compression hardly occurs for collisions with sufficiently low velocities. With an increase in E_{imp} , the compression of BCCAs begins at $E_{\text{imp}} \sim E_{\text{roll}}$ and ends at $E_{\text{imp}} \sim n_k E_{\text{roll}} \simeq N_{\text{total}} E_{\text{roll}}$. In the low-velocity limit, the gyration radius of the compound aggregate is given by that of the BCCA without restructuring. The BCCAs have the following relation between their total number of particles and gyration radius $r_{g,\text{BCCA}}$ (e.g., Mukai et al. 1992):

$$N_{\text{total}} \sim \left(\frac{r_{g,\text{BCCA}}}{r_1} \right)^{d_f}. \quad (52)$$

We prepare 10^4 sets of 2D BCCAs up to $N_{\text{total}} \simeq 2 \times 10^5$ through head-on sticking (see Fig. 4) and obtain for the 2D case,

$$N_{\text{total}} = 1.37 \left(\frac{r_{g,\text{BCCA}}}{r_1} \right)^{1.57}, \quad (53)$$

as shown in Figure 10. On the other hand, the gyration radius of 2D compact aggregates is given by

$$r_{g,\text{comp}} \sim r_1 N_{\text{total}}^{1/2} \quad (54)$$

for $N_{\text{total}} \gg 1$. Using equations (52) and (54), we can estimate the slope of the gyration radius to be

$$\frac{\log r_{g,\text{comp}} - \log r_{g,\text{BCCA}}}{\log(N_{\text{total}} E_{\text{roll}}) - \log E_{\text{roll}}} \simeq \frac{1}{2} - \frac{1}{d_f}. \quad (55)$$

Note that the slope is determined only by the fractal dimension d_f of the aggregates for large N_{total} . For $d_f = 1.57$, the slope equals -0.137 . The line with this slope is shown in Figure 8.

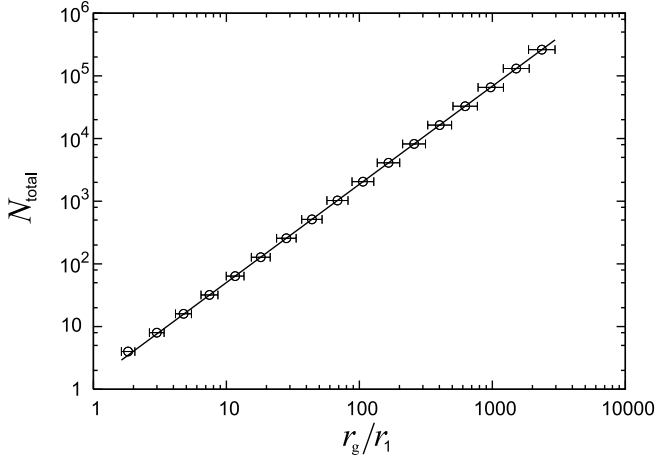


FIG. 10.—Number of particles in 2D BCCAs against their gyration radius. The circles represent the averaged data with error bars of 1σ , obtained by using 10,000 numerically produced BCCAs. A fitting line indicated by the solid line is given by $N_{\text{total}} = 1.37(r_g/r_1)^{1.57}$.

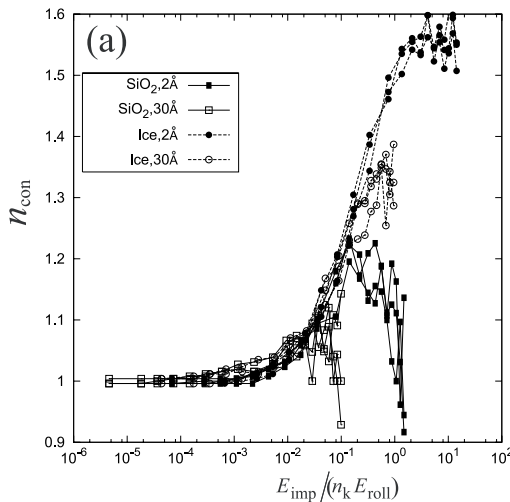
5.3. The Number of Contacts

Figure 11a shows that the number of contacts n_{con} per particle in the largest cluster increases with the impact energy. The number of contacts is another measure of aggregate compression. When the impact energy is smaller than E_{roll} , n_{con} hardly increases from the value of BCCAs without restructuring (≈ 1). When $E_{\text{imp}} \gtrsim E_{\text{roll}}$, on the other hand, n_{con} increases with E_{imp} through restructuring of the aggregate by rolling. Note that the number of contacts is irrelevant to both ξ_{crit} and grain materials, implying that n_{con} is scaled by $n_k E_{\text{roll}}$. Indeed, we find that n_{con} is expressed as

$$n_{\text{con}} - 1 = \left(\frac{E_{\text{imp}}}{n_k E_{\text{roll}}} \right)^{0.75} \quad (56)$$

for $E_{\text{imp}} \lesssim 0.1n_k E_{\text{roll}}$, as shown in Figure 11b.

For each parameter set, n_{con} begins to deviate from the relation (56) when the impact energy attains $\sim n_k E_{\text{break}}$. So, this deviation is due to disruption of the aggregate. The increase in n_{con} is suppressed by the aggregate disruption, implying that the degree of maximum compression is controlled by contact breaking in addition to particle rolling motion.



To see the dependency of the compression process on the aggregate size N_{total} , we plot n_{con} against the impact energy for various N_{total} in Figure 12. The number of contacts n_{con} per particle is almost independent of N_{total} for $N_{\text{total}} \geq 256$, while for small aggregates of $N_{\text{total}} = 16$ and 64 it is less than that for large aggregates. This property in small aggregates is simply due to a geometrical effect and is not related to the compression process. For small aggregates, the fraction of particles located on the outer edge of the aggregates is high. Particles located on the outer edge of an aggregate have a small number of contacts (initially, 1) compared to those located in the inner region of the aggregate (initially, 2). As a result, n_{con} for small aggregates appears to be small. Furthermore, the maximum value of n_{con} seems to depend on N_{total} (Fig. 12). This is also due to a geometrical effect in small aggregates. Consider a compact 2D aggregate composed of N particles, then the number of particles located on the edge is $\sim \sqrt{N}$. If the mean number of contacts per particle in the inner region of the compact aggregate is k , the maximum number of contacts per particle for the aggregate is evaluated to be

$$n_{\text{con, max}}(N) \sim \frac{k(N - \sqrt{N}) + \sqrt{N}}{N} = k - \frac{k-1}{\sqrt{N}}. \quad (57)$$

This relation indicates that $n_{\text{con, max}}$ approaches a certain value, $k \simeq 1.3-1.4$ for quartz and $k \simeq 1.6$ for ice, with increasing the number of particles, as is seen in Figure 12. The values of $n_{\text{con, max}}$ given by equation (57) are consistent with those shown in Figure 12. Therefore, we conclude that the aggregate size N_{total} does not affect the compression process for large N_{total} .

5.4. Degree of Maximum Compression

We have shown in § 5.3 (see Figs. 11 and 12) the behavior of the number of contacts, n_{con} , exhibits a characteristic dependence on $E_{\text{imp}}/(n_k E_{\text{roll}})$ that is irrelevant to the other parameters such as aggregate size N_{total} and material properties. However, the maximum values of n_{con} depend on the materials and ξ_{crit} . This difference in the degree of maximum compression can be explained by the ratio $E_{\text{roll}}/E_{\text{break}}$. Since a great number of contacts in aggregates start to be broken near the maximum compression, the resistance to breaking the contacts should be considered in addition to the resistance to rolling motion. Indeed, the maximum

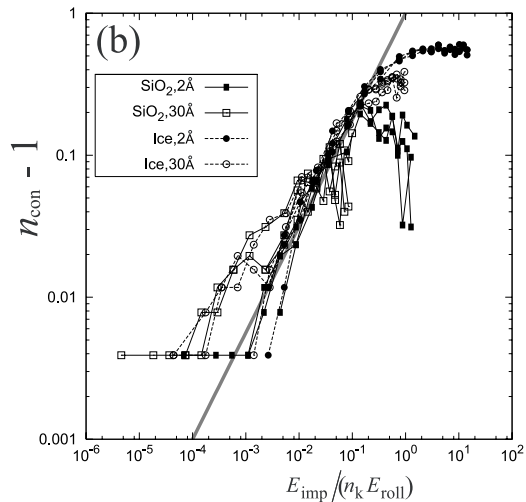


FIG. 11.—(a) Number of contacts n_{con} per particle in the largest cluster after impact vs. impact energy E_{imp} . (b) Log-log plot of $n_{\text{con}} - 1$ vs. $E_{\text{imp}}/(n_k E_{\text{roll}})$. The gray line in (b) shows a line given by $n_{\text{con}} - 1 = [E_{\text{imp}}/(n_k E_{\text{roll}})]^{0.75}$. The simulation setting represented by each symbol is the same as that in Fig. 7.

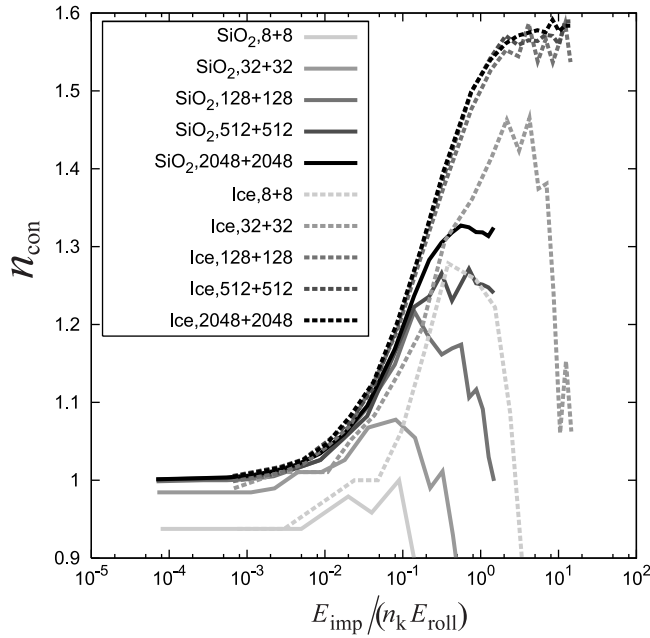


FIG. 12.—Number of contacts n_{con} per particle in the largest cluster vs. the impact energy for aggregates with different sizes. For all cases, we take $\xi_{\text{crit}} = 2 \text{ \AA}$ and average the outputs in three different initial aggregates produced by random numbers. Solid and dashed curves indicate the outcomes for quartz and ice aggregates, respectively. The gray scale for each curve corresponds to the number of particles (8, 32, 128, 512, and 2048) of the aggregates before impact.

value of the number of contacts decreases with increasing $E_{\text{roll}}/E_{\text{break}}$ and almost the same around $E_{\text{roll}}/E_{\text{break}} \simeq 20\text{--}30$ (see Fig. 11 and Table 3). As seen in Figure 13, the aggregates become apparently less compact with increasing $E_{\text{roll}}/E_{\text{break}}$. With a small value of $E_{\text{roll}}/E_{\text{break}}$, particles can be rolled enough while keeping their contacts, so that aggregates become compact. In contrast, with a large $E_{\text{roll}}/E_{\text{break}}$ such as quartz aggregates with $\xi_{\text{crit}} = 30 \text{ \AA}$, the aggregates break before becoming well compacted. As a result, the ratio $E_{\text{roll}}/E_{\text{break}}$ represents the difficulty of restructuring and compression.

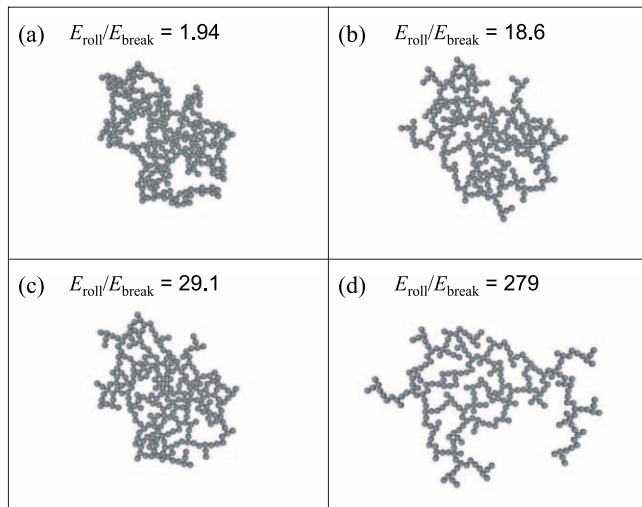


FIG. 13.—Collisional outcomes of aggregates at maximum compression for various values of $E_{\text{roll}}/E_{\text{break}}$. The parameters are (a) ice with $\xi_{\text{crit}} = 2 \text{ \AA}$ and $v_{\text{imp}} = 5.7v_0$, (b) quartz with $\xi_{\text{crit}} = 2 \text{ \AA}$ and $v_{\text{imp}} = 5.7v_0$, (c) ice with $\xi_{\text{crit}} = 30 \text{ \AA}$ and $v_{\text{imp}} = 8.5v_0$, and (d) quartz with $\xi_{\text{crit}} = 30 \text{ \AA}$ and $v_{\text{imp}} = 5.7v_0$. The initial aggregate consists of 128 particles, as shown in Fig. 4.

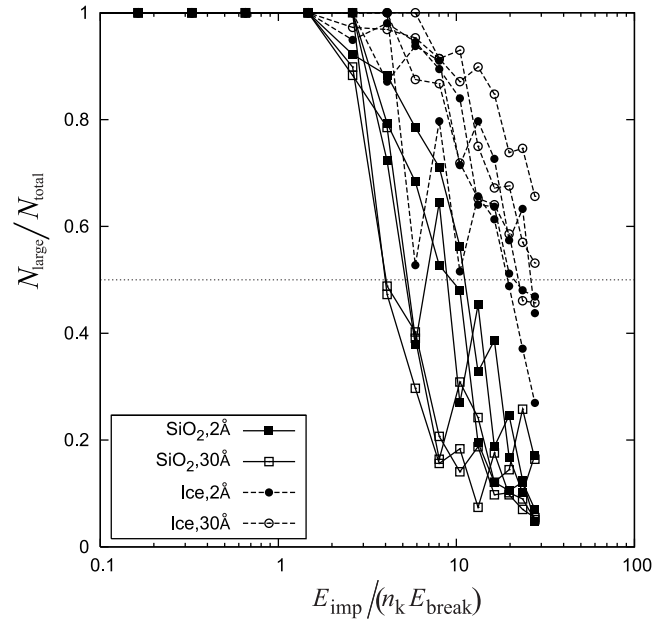


FIG. 14.—Ratio of the number of particles in the largest cluster, N_{large} , to the total number of particles, N_{total} , as a function of the impact energy E_{imp} . The simulation setting represented by each symbol is the same as that shown in Fig. 7. The size of each aggregate in collision is $N_{\text{total}} = 256$.

5.5. Largest Cluster Size in the Disruption Regime

Figure 14 shows the ratio of the largest cluster size $N_{\text{large}}/N_{\text{total}}$ as a function of impact energy normalized by $n_k E_{\text{break}}$ for the collisions of aggregates composed of 128 particles. If the aggregates are disrupted by the collision, the ratio $N_{\text{large}}/N_{\text{total}}$ becomes less than unity. We call disruption with $N_{\text{large}}/N_{\text{total}} \leq 0.5$ a catastrophic disruption. We can see a clear trend that disruption occurs at impact energies larger than $\sim 3n_k E_{\text{break}}$. Catastrophic disruption occurs when the impact energy becomes larger than $\sim 10n_k E_{\text{break}}$. These results are in agreement with the DT recipe that the disruption process would be scaled by $n_k E_{\text{break}}$. However, there seems to be a tendency that quartz aggregates are disrupted easier than ice. This tendency cannot be explained by the DT recipe.

To examine the size dependence of the disruption process, we plot the largest cluster size for various N_{total} in Figure 15a. The ratio $N_{\text{large}}/N_{\text{total}}$ increases with N_{total} (≤ 1024) at each value of $E_{\text{imp}}/(n_k E_{\text{break}})$ (i.e., at each collision velocity). This indicates that large aggregates tend to be harder against disruption up to $N_{\text{total}} = 1024$.

The outcomes for collisions of aggregates of $N_{\text{total}} = 4096$ differ from the tendency in the cases of $N_{\text{total}} \leq 1024$. To clarify the reason of the difference, we plot each result for collisions of aggregates of $N_{\text{total}} = 4096$ in Figure 15b. The results indicate that the disruption curves strongly depend on the initial aggregate structures. For one of the initial structures of the aggregates represented by the lines with circles in Figure 15b, they are hard against disruption compared to the other small aggregates, suggesting that large dust aggregates become so strong against disruption that they can grow efficiently. For the other initial structures, however, the aggregates are disrupted easily. Examples of the snapshots of these collisions are depicted in Figure 16 showing that aggregates are hard to be disrupted in the case of upper panels, while they tend to split into some clusters when disrupted in the case of lower panels. The results indicate that the disruption outcome depends on the initial structure (and collision direction) of the aggregates if N_{total} is larger than thousands. If the collision cross section is small (upper case in Fig. 16),

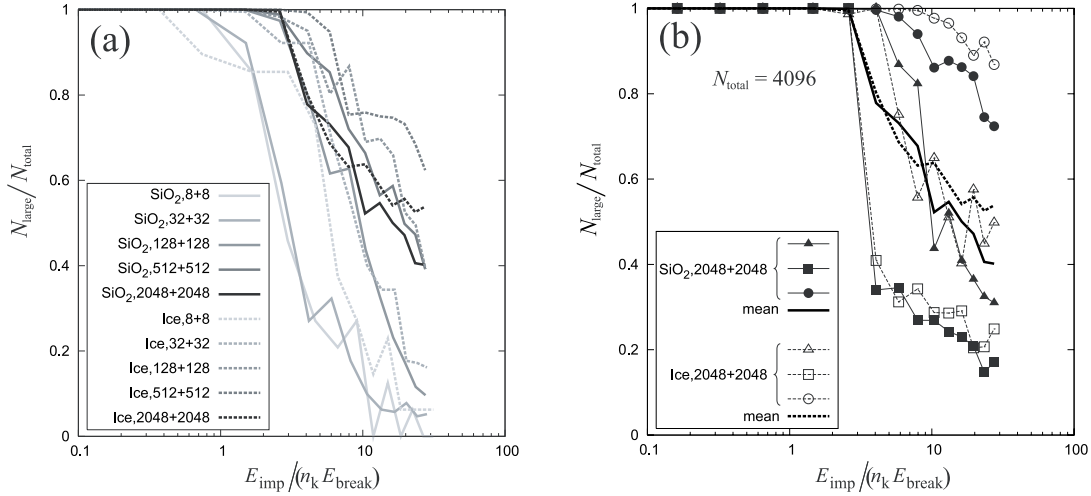


FIG. 15.—(a) $N_{\text{large}}/N_{\text{total}}$ vs. $E_{\text{imp}}/(n_k E_{\text{break}})$ for aggregates with different sizes. For all cases, we take $\xi_{\text{crit}} = 2 \text{ \AA}$ and average the outputs in three different initial aggregates produced by random numbers. Solid and dashed curves indicate the outcomes for quartz and ice aggregates, respectively. The gray scale for each curve corresponds to the number of particles (8, 32, 128, 512, and 2048) of the aggregate before impact. (b) Same as (a), but for the aggregates of $N_{\text{total}} = 4096$ of three different initial aggregates represented by the lines with different symbols.

particles concentrate into a narrow region and make a compact aggregate. On the other hand, if collision cross section is large (lower case in Fig. 16), disruption occurs at many points widely distributed in the aggregates, and they tend to split into some clusters. If the former case is dominant in aggregate collisions, aggregates become harder against disruption with increasing the number of particles.

6. SUMMARY AND CONCLUDING REMARKS

We carried out numerical simulations of head-on collisions of 2D BCCAs to study the compression and disruption processes in their growth. For the simulation, we developed the particle interaction model based on the works by Johnson et al. (1971) and Dominik & Tielens (1995, 1996, 1997). We modified their formulations by introducing potentials so that the energy conservation is well guaranteed in the computation. Compared to the similar numerical simulation by Dominik & Tielens (1997) our simulation treated a large number of particles and various initial structures of the aggregates, allowing statistical discussions of the compression and disruption processes of aggregate collision.

The compression process is represented by the change in the gyration radius and the number of contacts of aggregates. The gyration radius is kept at that of the BCCA without restructuring for impact energies $E_{\text{imp}} \lesssim E_{\text{roll}}$. When E_{imp} becomes large enough,

the gyration radius decreases reflecting aggregate compression. We obtain the following empirical relation:

$$r_g = r_1 \sqrt{N_{\text{large}}} \left(\frac{E_{\text{imp}}}{n_k E_{\text{roll}}} \right)^{-0.137} \quad (E_{\text{roll}} \lesssim E_{\text{imp}} \lesssim n_k E_{\text{roll}}). \quad (58)$$

The gyration radius attains its minimum value when the impact energy is nearly equal to the energy necessary to roll all contacts, $n_k E_{\text{roll}}$. This result confirms that of Dominik & Tielens (1997), who showed that the maximum compression of an aggregate occurs when the impact energy becomes $n_k E_{\text{roll}}$. The number of contacts increases with impact energy and achieves its maximum value at $E_{\text{imp}} \sim n_k E_{\text{break}}$. For the number of contacts per particles, we also obtain an empirical relation:

$$n_{\text{con}} = 1 + \left(\frac{E_{\text{imp}}}{n_k E_{\text{roll}}} \right)^{0.75} \quad (E_{\text{imp}} \lesssim n_k E_{\text{break}}). \quad (59)$$

As a result, the change in the gyration radius $r_g/(r_1 N_{\text{large}}^{1/2})$ and the number of contacts per particles of aggregates can be scaled by $E_{\text{imp}}/(n_k E_{\text{roll}})$, irrespective of the initial conditions and the parameters. We find that the degree of maximum compression depends on the ratio of the rolling energy to the breaking energy, $E_{\text{roll}}/E_{\text{break}}$. This suggests that ice aggregates become more compact than quartz aggregates. The energy E_{roll} is one of the key parameters that characterize the compression of aggregates at collisions and depends on the critical rolling displacement ξ_{crit} . We urge laboratory measurements of ξ_{crit} for small ($\sim 0.1 \mu\text{m}$) ice and silicate particles when one applies the scaling to dust collisions in protoplanetary disks. Our results show that catastrophic disruption occurs when the impact energy becomes greater than $\sim 10 n_k E_{\text{break}}$, which is in agreement with the results obtained by Dominik & Tielens (1997). We examined the dependence of the disruption on the size N_{total} of aggregates. For the aggregate size $N_{\text{total}} \lesssim 4000$ dealt with in our simulation, we find that the aggregates tend to be hard against disruption as N_{total} increases. This suggests that dust aggregates could grow efficiently, although the anisotropy of the collision cross section plays a role for the aggregates of $N_{\text{total}} \simeq 4000$.

The experiments by Poppe et al. (2000) show that the sticking velocity, the maximum collision velocity allowing two grains to

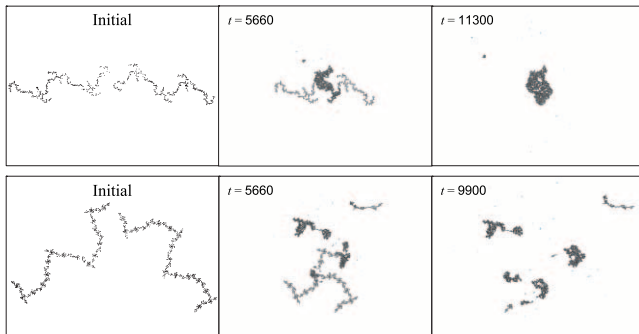


FIG. 16.—Two collisional snapshots (*upper and lower*) of aggregates with different initial structures. Each of the initial aggregates is composed of 2048 ice particles with $\xi_{\text{crit}} = 2 \text{ \AA}$. The impact energies are $E_{\text{imp}} = 10.4 n_k E_{\text{break}}$ for both collisions. Time t is in units of t_c .

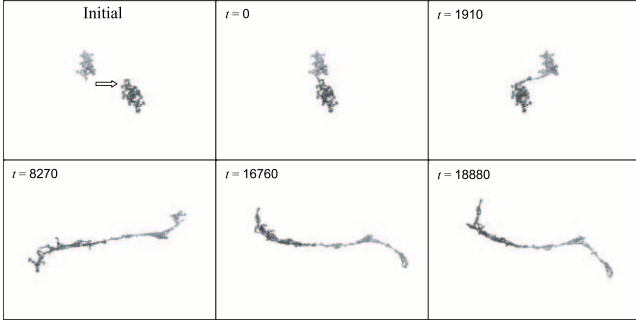


FIG. 17.— Snapshots of an offset collision of 3D BCCAs composed of 1024 ice particles with $\xi_{\text{crit}} = 2 \text{ \AA}$. The impact velocity is $5.7v_0$ ($E_{\text{imp}} = 2.6n_k E_{\text{break}}$). Time t is in units of t_c . In contrast to the head-on collisions, the aggregate formed by the offset collision is elongated significantly, and thus, its gyration radius greatly increases.

stick to each other, is higher by an order of magnitude than the predictions of theoretical works (Chokshi et al. 1993; Dominik & Tielens 1997). Poppe et al. (2000) claim that such high sticking velocity is caused by multiple contacts due to irregular shape or surface roughness of the grains, while the theoretical works assume spherical particles of smooth surface. This conjecture may be examined in the future by applying the present code with representing grains of irregular shape or those having a rough surface by assemblages of small particles.

Paszun & Dominik (2006) report that the rotation of aggregates before collision plays an important role in determining the structure of the aggregate formed. We suggest that an offset collision is also important. Figure 17 shows our preliminary numerical result of an offset collision of 3D BCCAs. New factors introduced by the offset collision are (1) the angular momentum of the system and (2) inefficient energy dissipation compared to head-on collisions. As seen in Figure 17, these factors give rise to a much elongated aggregate, which is not observed in head-on collisions in our simulation. In offset collisions, the change in the aggregate structure such as the gyration radius becomes complex compared to the case of head-on collisions. We shall discuss 3D simulations to reveal the difference between 2D and 3D and the influence of offset collisions in a subsequent paper.

We thank S. Sirono and M. Arakawa for valuable discussions, and an anonymous reviewer for useful comments. We are grateful to T. Chigai for technical support on computer setup. This study was supported by the Grant-in-Aid for Scientific Research on Priority Areas “Development of Extrasolar Planetary Science” (16077203), and “Astrophysical Observations of New Phases of the Interstellar Gas at Sub-mm and THz Regions” (18026001), MEXT, Japan, and by the Grant-in-Aid from JSPS (18540227).

APPENDIX

CORRECTION OF CONTACT POINTER

We describe a detailed procedure to obtain a corrected contact pointer \mathbf{n}_1^c of the particle 1 given by equation (42). As mentioned in the text, inelastic sliding occurs at $t = t_{\text{ie}}$, and the increment of the sliding displacement from the critical position is given by $\Delta\zeta = \zeta(1 - \zeta_{\text{crit}}/|\zeta|)$. As a result, the contact pointer $\mathbf{n}_1(t_{\text{ie}})$ should be replaced by \mathbf{n}_1^c . The apparent correction is given by

$$l = \left| \frac{\Delta\zeta}{2r_1} \right|. \quad (\text{A1})$$

The true length of the correction, however, is not given by l , because the length of the corrected contact pointer \mathbf{n}_1^c must be normalized to unity and the amount of the correction after the normalization becomes different from l if \mathbf{n}_1^c is given by $\mathbf{n}_1(t_{\text{ie}}) - \Delta\zeta/(2r_1)$. Let l' be the true length of the correction and \mathbf{n}_1^c be expressed by

$$\mathbf{n}_1^c(t_{\text{ie}}) = \mathbf{n}_1(t_{\text{ie}}) - \frac{\Delta\zeta}{2r_1} \frac{l'}{l}, \quad (\text{A2})$$

where $\alpha = l'/l$ in equation (42). The correction factor $\alpha = l'/l$ can be calculated as follows (see Fig. 18). From Figure 18, we have

$$\cos \vartheta_1 - \cos(\vartheta_1 + \vartheta_2) = l, \quad (\text{A3})$$

$$\cos \vartheta_1 - \sqrt{l'^2 - 2l' \cos \vartheta_1 + 1} \cos(\vartheta_1 + \vartheta_2) = l', \quad (\text{A4})$$

where

$$\cos \vartheta_1 = \frac{\mathbf{n}_1(t_{\text{ie}}) \cdot \Delta\zeta}{|\Delta\zeta|}, \quad (\text{A5})$$

and ϑ_2 is an angle between \mathbf{n}_1 and \mathbf{n}_1^c . Equations (A3) and (A4) yield

$$l' = \cos \vartheta_1 - \frac{(\cos \vartheta_1 - l) \sin \vartheta_1}{\sqrt{1 - (\cos \vartheta_1 - l)^2}}. \quad (\text{A6})$$

Since $\vartheta_2 \ll 1$ and $l \ll \cos \vartheta_1$, l' is given by

$$l' = l \left(1 + \frac{1}{\tan^2 \vartheta_1} \right) + O(l^2). \quad (\text{A7})$$

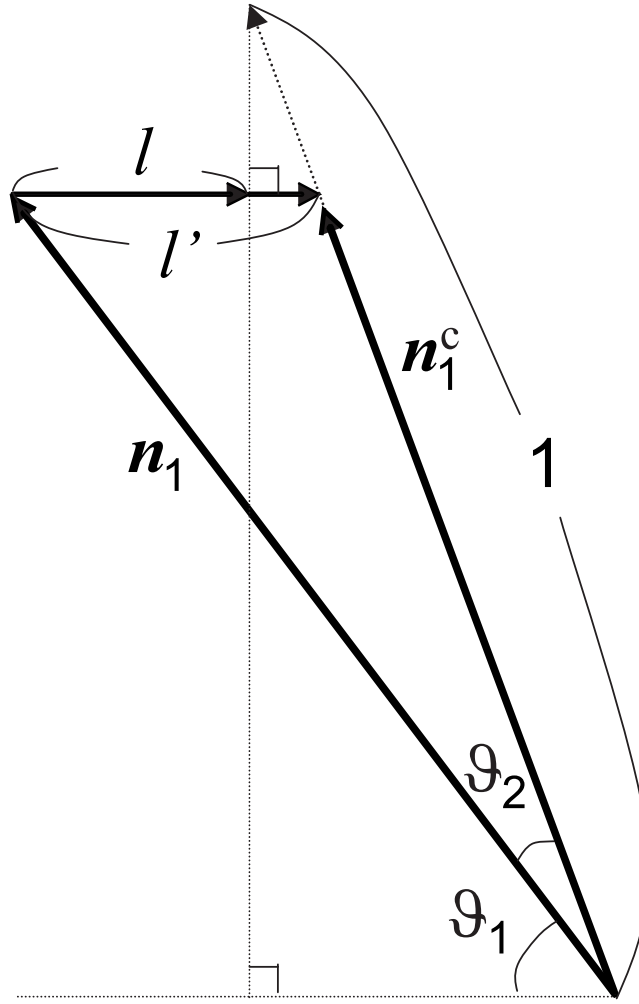


FIG. 18.—Schematic view of $\mathbf{n}_1(t_{ic})$ and $\mathbf{n}_1^c(t_{ic})$. The apparent correction vector has a length of l , while the true correction vector has a length of l' .

Thus, the correction factor α is

$$\alpha = \frac{l'}{l} \simeq 1 + \frac{1}{\tan^2 \vartheta_1}, \quad (\text{A8})$$

with reasonable accuracy.

REFERENCES

- Adachi, I., Hayashi, C., & Nakazawa, K. 1976, *Prog. Theor. Phys.*, 56, 1756
 Blum, J. 2004, in *ASP Conf. Ser. 309, Astrophysics of Dust*, ed. A. N. Witt, G. C. Clayton, & B. T. Draine (San Francisco: ASP), 369
 Blum, J., & Wurm, G. 2000, *Icarus*, 143, 138
 Chokshi, A., Tielens, A. G. G. M., & Hollenbach, D. 1993, *ApJ*, 407, 806
 Dominik, C., & Nübold, H. 2002, *Icarus*, 157, 173
 Dominik, C., & Tielens, A. G. G. M. 1995, *Philos. Mag. A*, 72, 783
 ———. 1996, *Philos. Mag. A*, 73, 1279
 ———. 1997, *ApJ*, 480, 647
 Goldstein, H. 1950, *Classical Mechanics* (Reading: Addison-Wesley)
 Heim, L.-O., Blum, J., Preuss, M., & Butt, H.-J. 1999, *Phys. Rev. Lett.*, 83, 3328
 Israelachvili, J. 1992, *Intermolecular and Surface Forces* (2nd ed.; London: Academic Press)
 Johnson, K. L. 1987, *Contact Mechanics* (Cambridge: Cambridge Univ. Press)
 Johnson, K. L., Kendall, K., & Roberts, A. D. 1971, *Proc. R. Soc. London A*, 324, 301
 Kempf, S., Pfalzner, S., & Henning, T. K. 1999, *Icarus*, 141, 388
 Meakin, P. 1991, *Rev. Geophys.*, 29, 317
 Min, M., Dominik, C., Hovenier, J. W., de Koter, A., & Waters, L. B. F. M. 2006, *A&A*, 445, 1005
 Min, M., Hovenier, J. W., & de Koter, A. 2003, *A&A*, 404, 35
 ———. 2005, *A&A*, 432, 909
 Mukai, T., Ishimoto, H., Kozasa, T., Blum, J., & Greenberg, J. M. 1992, *A&A*, 262, 315
 Nakagawa, Y., Nakazawa, K., & Hayashi, C. 1981, *Icarus*, 45, 517
 Ormel, C. W., Spaans, M., & Tielens, A. G. G. M. 2007, *A&A*, 461, 215
 Ossenkopf, V. 1993, *A&A*, 280, 617
 Paszun, D., & Dominik, C. 2006, *Icarus*, 182, 274
 Poppe, T., Blum, J., & Henning, T. 2000, *ApJ*, 533, 454
 Stognienko, R., Henning, T., & Ossenkopf, V. 1995, *A&A*, 296, 797
 Tanaka, H., Himeno, Y., & Ida, S. 2005, *ApJ*, 625, 414
 Wada, K., Senshu, H., & Matsui, T. 2006, *Icarus*, 180, 528
 Weidenschilling, S. J. 1980, *Icarus*, 44, 172
 ———. 1984, *Icarus*, 60, 553
 Weidenschilling, S. J., & Cuzzi, J. N. 1993, in *Protostars and Planets III*, ed. E. H. Levy & J. I. Lunine (Tucson: Univ. Arizona Press), 1031
 Weidenschilling, S. J., & Ruzmaikina, T. V. 1994, *ApJ*, 430, 713
 Wright, E. L. 1987, *ApJ*, 320, 818